ROYAL SOCIETY OF CHEMISTRY

PAPER

Check for updates

Demonstration of a 50 cm² BiVO₄ tandem photoelectrochemical-photovoltaic water splitting device†

Ibbi Y. Ahmet, [ID] ‡[a] Yimeng Ma, [ID] ‡[a] Ji-Wook Jang,[a] Tobias Henschel,[b] Bernd Stannowski, [ID] [b] Tânia Lopes, [ID] [c] António Vilanova, [ID] [c] Adélio Mendes, [ID] [c] Fatwa F. Abdi [ID] *[a] and Roel van de Krol [ID] *[a]

In this paper, we demonstrate a new benchmark for a large area photoelectrochemical–photovoltaic (PEC–PV) solar water splitting device with a metal oxide-based top absorber. The stand-alone 50 cm² device consists of cobalt phosphate-coated tungsten-doped BiVO₄ (CoP$_i$/W:BiVO₄) photoanodes combined with series-connected silicon heterojunction (SHJ) solar cells. We highlight the performance limitations for large area BiVO₄ photoanodes and present initial attempts in overcoming these challenges. Specific challenges encountered are (i) the high resistivity of the FTO substrate, (ii) non-uniform CoP$_i$ deposition, and (iii) limited ionic conductivity of the 0.1 M phosphate buffer electrolyte typically used for small area BiVO₄ devices. The former two problems were overcome by applying Ni lines to the FTO substrate, and the latter to some extent by increasing the electrolyte concentration to 2.0 M. Despite the high buffer concentration, the overall performance of the large area photoelectrodes was found to be limited by H⁺/OH⁻ transport in this near-neutral pH electrolyte. This limitation results in H⁺/OH⁻ depletion towards the center of the large area electrode and significant potential drop, which can be overcome by implementing a cell design with a small electrode-area-to-electrolyte-volume ratio. Our optimized photoanodes were then integrated into tandem PEC–PV devices in either a single or dual photoanode configuration. These 50 cm² PEC–PV devices demonstrate solar to hydrogen (STH) efficiencies of 1.9% (single CoP$_i$/W:BiVO₄ and 2-series connected SHJ cells) and 2.1% (dual CoP$_i$/W:BiVO₄ and 2-series connected SHJ cells). Optimized small area (0.24 cm²) PEC–PV devices based on a similar configuration show a STH efficiency of up to 5.5%. Our results illustrate the challenges involved in the scale-up of solar water splitting devices and underline the importance of increased electrochemical engineering efforts in this developing field.

Introduction

Solar water splitting is expected to be a central component for any future fossil fuel-free energy infrastructure that relies on chemical fuels as an energy vector.[1] The produced hydrogen can either be used directly as a chemical fuel, or as a feedstock to produce other fuels or fine chemicals. Direct photoelectrochemical (PEC) water splitting (*i.e.*, where light absorption and chemical reactions occur in the same device) offers several advantages over photovoltaic-driven electrolysis, such as the possibility of using earth-abundant catalysts due to lower operating current density and utilizing waste heat to enhance the electrochemical reaction kinetics.[1] Among the various light absorber materials available as photoelectrodes in a practical PEC device, which need to be low cost, scalable, stable and highly efficient, metal oxides have attracted much attention as promising candidates. Bismuth vanadate (BiVO₄) is one of these promising metal oxides and can be used as a photoanode.[2,3] A particularly interesting feature of BiVO₄ is its relatively low onset potential, which is typically ∼0.2–0.4 V$_{RHE}$ (potential with respect to reversible hydrogen electrode, RHE) with appropriate surface modifications.[4,5] We, and others, have reported various strategies to modify and improve the performance of BiVO₄ photoanodes, including homogeneous and gradient doping,[5,6] surface modification with co-catalysts,[5–7] formation of hetero-/

homo-junctions,[8,9] and nano-structuring.[4] Photocurrent densities as high as 6.7 mA cm^{-2} at 1.23 V$_{RHE}$ in nanostructured heterojunction samples have been reported using tungsten oxide nanorods as scaffolds for the BiVO$_4$ top layer with cobalt phosphate (CoP$_i$) surface modification.[8] This is very close to the theoretical maximum AM 1.5G photocurrent density that can be achieved with BiVO$_4$ ($\sim$7.5 mA cm^{-2} based on its 2.4 eV bandgap).

Building on the impressive progress in PEC materials development in the past 10–15 years, focus has now turned towards fabricating practical stand-alone PEC water splitting devices[10] and understanding the long-term stability of this material.[11] Integrated tandem devices based on the combination of a BiVO$_4$-based photoanode as a wide-bandgap top absorber and various types of bottom absorbers have been reported in the literature. The bottom absorbers are usually photovoltaic (PV) cells based on *e.g.* Si,[6,13,25] organic PV (OPV),[19] dye-sensitized solar cells (DSSC),[16] or lead-halide perovskites,[14,18,21,22] but other metal oxide-based photocathodes[12,23] have also been used. An overview of these tandem devices is shown in Table 1. Moderate efficiencies are feasible with such modular PEC–PV or PEC–PEC device configurations, with more than half of the devices in Table 1 showing STH efficiencies between 4-8%. Many of these devices employ low-cost and scalable deposition techniques based on solution processing, such as spray pyrolysis and drop-casting. Although the efficiencies are still much lower than the 20–30% benchmark of PV-driven electrolysis (PV–EC) devices,[26,27] the potential for cheaper renewable hydrogen through device integration, the use of stable and abundant materials, and the ability to use waste heat

to accelerate the electrochemical reactions provide a strong motivation to continue efforts in developing metal oxide-based solar water splitting devices.

With STH efficiencies of PEC–PV water splitting devices approaching 10%, the next step is to move beyond laboratory experiments and demonstrate large area PEC–PV water splitting devices. Several modeling and simulation papers have indeed investigated device scale-up,[28–30] but most experimental studies thus far (see Table 1) have only demonstrated devices with active areas less than 1 cm.² Notable exceptions are the work of Turan *et al.*, who reported a 64 cm² PV-EC module (consisting of identical 13 base units) based on Si heterojunction solar cells and nickel catalysts with 3.9% STH efficiency,[24] and the impressive 1.6 m² PEC–PV system reported by the ARTIPHYCTION consortium. The latter is based on combining BiVO$_4$ photoanodes side-by-side with silicon solar cells (*i.e.*, it is not a true tandem system) to form a total device area of 64 cm².[25] The efficiency of this system was not reported. Although no standalone device was demonstrated, Lu *et al.* very recently reported the fabrication of cobalt-doped BiVO$_4$ (Co:BiVO$_4$) photoanodes with an area of up to 300 cm². They showed that simply increasing the electrode area decreases the photocurrent by a factor of $\sim$5.[31] These types of losses have been observed elsewhere in the scale up of metal oxide photoanodes.[32] However, no detailed analysis of the underlying reasons for the lower photocurrent densities for the large area photoanodes (25 and 300 cm²) as compared to the smaller area (1 cm²) was made.

These studies show that efforts on large-area demonstrator devices need to be intensified, as they will reveal scale-up challenges and limitations that would otherwise go unnoticed

Table 1 Summary of reported solar water splitting devices based on BiVO$_4$ and PV/photocathode configurations

Photoanode (top absorber)	Bottom absorber	Area per cm²	$\sim$pH	η_{STH}/%	Year	Ref.
Small area ($\leq$1 cm²)						
Gradient-W:BiVO$_4$ (200 nm)/CoP$_i$	2-jn a-Si	0.28	7	4.9	2013	5
Gradient-W:BiVO$_4$ (200 nm)/CoP$_i$	Au/Cu$_2$O/AZO/TiO$_2$/RuO$_x$	0.28	7	0.5	2014	12
Gradient-W:BiVO$_4$ (250 nm)/CoP$_i$	2-jn micromorph a-Si/μc-Si	0.28	7	5.2	2014	13
BiVO$_4$/CoP$_i$	Lead halide perovskite PV	0.54	7	2.5	2015	14
BiVO$_4$/NiOOH/FeOOH	CuGa$_3$Se$_5$	—	7	0.7	2015	15
WO$_3$ nanorods/BiVO$_4$/CoP$_i$	GaAs/InGaAsP	0.16	7	8.1	2015	8
WO$_3$/BiVO$_4$	DSSC	—	7	5.7	2015	16
BiVO$_4$/NiOOH/FeOOH and α-Fe$_2$O$_3$/NiFeO$_x$ (dual)	c-Si	0.3	7	7.7	2016	15
DBR/BiVO$_4$/NiOOH/FeOOH	DSSC	—	7	7.1	2016	17
Mo:BiVO$_4$ nano-cones/Fe(Ni)OOH	Lead halide perovskite PV	0.25	7	6.2	2016	18
BiVO$_4$/NiOOH/FeOOH	OPV	0.036	7	2.2	2017	19
BiVO$_4$/CoO$_x$/NiO	(ZnSe)$_{0.85}$(CuIn$_{0.7}$Ga$_{0.3}$Se$_2$)$_{0.15}$	1	9.5	1.0	2017	20
SnO$_2$/WO$_3$/BiVO$_4$/CoO$_x$	Lead halide perovskite PV	0.14	7	3.5	2017	21
2 $\times$ BiVO$_4$/NiOOH/FeOOH	Lead halide perovskite PV	—	9.5	6.5	2018	22
H,Mo:BiVO$_4$/NiFeO$_x$	FTO/Cu/Cu$_2$O/Ga$_2$O$_3$/TiO$_2$/RuO$_x$	0.25–0.8	9	3.0	2018	23
2 $\times$ H,W:BiVO$_4$/CoP$_i$ (dual)	**2 $\times$ SHJ Si**	**0.24**	**7**	**5.5**		**This work**
2 $\times$ H,W:BiVO$_4$/CoP$_i$ (dual)	**3 $\times$ SHJ Si**	**0.24**	**7**	**6.3**		**This work**
Large area (>1 cm²)						
Si PV/Ni foam^a	Si PV + Ni Foam (cathode)	64	$\sim$13	3.9	2016	24
Mo–BiVO$_4$/CoP$_i$	Si PV^b	16 000	7	—	2017	25
2 $\times$ H,W:BiVO$_4$ or W:BiVO$_4$/CoP$_i$ (dual)	**2 $\times$ SHJ Si**	**50**	**7**	**2.1**		**This work**

^{a} PV-EC device, without a semiconductor–electrolyte junction. ^{b} Not a true tandem configuration, since Si PV cell and BiVO$_4$ photoanode were placed side-by-side.

in small scale laboratory experiments. For example, the efficiency of small area PEC–PV devices is mainly determined by the performance of the photoelectrode, surface co-catalyst, and PV cell. For larger area PEC–PV systems, however, factors like electrode and electrolyte conductivity, photoelectrode uniformity, pH gradient, and light scattering caused by gas bubbles may dominate the overall device performance.

In this paper, we report the first large area (50 cm^2) stand-alone PEC–PV water splitting tandem device based on a BiVO$_4$ photoanode and silicon heterojunction solar cells. Using a single-nozzle spray pyrolysis system, uniform deposition of BiVO$_4$ thin films with areas ranging from 1 cm^2 up to 100 cm^2 can be obtained by simply adjusting the carrier gas flow rate, thus making it a suitable technique for low-cost large area fabrication. We compare the performance of the large area BiVO$_4$ photoanode with the small area equivalent, and find that the substrate and electrolyte conductivity limit the performance of the large-area photoanode. By electrochemical engineering we were able to overcome the electronic and part of the ionic conductivity losses and achieve an AM1.5G photocurrent of $\sim$1.7 mA cm^{-2} at 1.23 V$_{RHE}$ using 50 cm^2 1% W-doped BiVO$_4$ dual photoanodes.[33] Further improvement of this large-scale photoanode is currently hindered by the limited proton conductivity in the electrolyte. The 'dual photoanode' configuration was then combined with two series-connected Si heterojunction (SHJ) solar cells in a tandem configuration to construct a large area stand-alone PEC–PV water splitting device with an STH efficiency of 2.1%. While this is still lower than the 5.5% STH efficiency we achieve for the corresponding small area devices (using two series-connected SHJ), the active area is more than two orders of magnitude larger. The 50 cm^2 device we demonstrate here represents a new benchmark for large area PEC–PV solar water splitting tandem device with a metal oxide-based top absorber.

Results and discussion

1. PEC performance of 50 cm^2 BiVO$_4$ photoanode for sulfite oxidation

Fig. 1 shows the PEC performance of typical small area (0.24 cm^2) and large area (50 cm^2) W-doped BiVO$_4$ photoanodes. In order to eliminate any charge transfer limitations, 0.5 M Na$_2$SO$_3$ was added to the 0.1 M KP$_i$ buffer (pH 7) electrolyte as a hole scavenger. Sulfite has been shown to inhibit surface recombination and promote charge transfer to the electrolyte due to the more favorable thermodynamics and faster reaction kinetics.[6,34] As seen in Fig. 1, there is a significant discrepancy in the photocurrent density between the small and large area samples. The optimized small area W:BiVO$_4$ samples can produce a photocurrent of $\sim$3.3 mA cm^{-2} at 1.23 V$_{RHE}$ with a photocurrent onset potential of $\sim$0.4 V$_{RHE}$. In contrast, the photocurrent density for a typical large area (50 cm^2) W:BiVO$_4$ sample is only $\sim$1.2 mA cm^{-2} at 1.23 V$_{RHE}$. The main causes of the $\sim$65% loss in photocurrent and possible measures to avoid it are the main focus of this paper and are discussed below.

The drop in the photocurrent is presumably caused by ohmic losses in the system due to *e.g.* resistance of the FTO substrate,
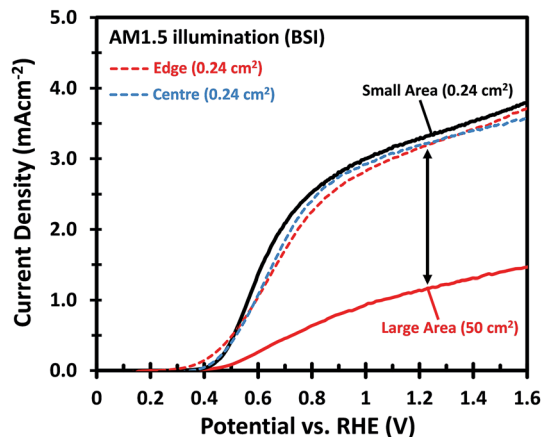

Fig. 1 The current density–voltage (*J*–*V*) curves of a small area (1 × 2 cm^2) W:BiVO$_4$ photoanode with an illuminated area of 0.24 cm^2 (black), compared to the large area (7 × 12 cm^2) W:BiVO$_4$ photoanode with an illuminated area of 50 cm^2 (red). The dashed curves show the *J*–*V* plots from the small W:BiVO$_4$ pieces (1 × 2 cm^2) cut from the centre and edge of the 50 cm^2 sample, with an illuminated area of 0.24 cm^2. The electrolyte consists of 0.5 M Na$_2$SO$_3$ and 0.1 M KP$_i$ buffer in deionized water with pH of 7. BSI: back-side illuminated.

finite conductivity of the electrolyte solution, and/or contact resistance(s). Since detailed modeling of these losses typically requires 2D numerical calculations, we first consider a simple model that captures all losses in the form of a single internal resistance, R_{int}. Using this model, which is described in more detail in ESI Note S1,† and assuming that the photocurrent density is the same everywhere and equal to that of the small area sample of Fig. 1, we calculated the expected photocurrent for a 50 cm^2 photoelectrode for different values of R_{int}. The results are shown in Fig. 2. The curves show a reasonable overlap with the measured data for an actual 50 cm^2 BiVO$_4$ photoelectrode (solid red curve) for an internal resistance value
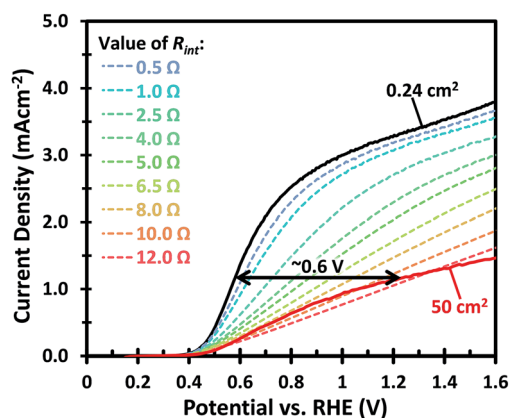

Fig. 2 The *J*–*V* curves of small (solid black) and large (solid red) W:BiVO$_4$ photoanodes measured in 0.5 M Na$_2$SO$_3$ + 0.1 M KP$_i$ pH 7 buffer under AM 1.5G illumination. These curves are compared with the calculated *J*–*V* curves of a 50 cm^2 W:BiVO$_4$ photoanode (dashed lines) with the same performance as the small area sample, but subjected to different resistances from 0.5 to 12 Ω.

of $\sim$10 Ω. At a potential of 1.23 V *vs.* RHE the voltage loss in the 50 cm^2 photoanode is about 0.6 V (see arrow in Fig. 2), consistent with current density at this potential (1.2 mA cm^{-2} $\times$ 50 cm^2 $\times$ 10 Ω $\approx$ 0.6 V).

1.1 Substrate conductivity. The internal resistance of $\sim$10 Ω is comparable to the sheet resistance of the FTO (7 Ω sq^{-1}). It is, therefore, tempting to conclude that the losses are due to the FTO. The 1.4$\times$ larger value could then be explained by the rectangular shape of the photoelectrode (7 $\times$ 12 cm^2). Carver *et al.* have indeed identified resistive losses in the FTO substrate as a crucial factor that may limit the performance of a large area (100 cm $\times$ 100 cm) photoelectrode.[35] To determine if this is also the case for our (much smaller) BiVO$_4$ photoelectrodes, a DC conductivity model was utilized to determine the potential drop across the FTO substrate for the small and large area photoanodes. The modeling approach we used is similar to the one used by Carver *et al.*, with the important addition of considering anisotropy in our model (see ESI Note S2† for detailed description of the model and simulation).[35] Fig. 3a and b show the simulated potential drops across the large (50 cm^2) area photoanode, calculated for a photocurrent density of 3 mA cm^{-2}. Fig. 3a shows that with contacts only around the edges of a large area photoanode (5 $\times$ 10 cm^2), the potential drop increases towards the center of the photoanode reaching a maximum of 62 mV. In contrast, as shown in Fig. S3,† the small area (0.24 cm^2) sample with the same current density only exhibits a maximum potential drop of 2 mV (*i.e.*, $\sim$30-fold smaller). The value calculated for the large area photoelectrode (62 mV at 3 mA cm^{-2}) is more than an order of magnitude smaller than the voltage drop

calculated with the simple internal resistance model described above (0.6 V at 1.2 mA cm^{-2}, Fig. 2). From this, we conclude that the similarity between the estimated "internal resistance" ($\sim$10 Ω) and the sheet resistance of the FTO is misleading and that the main resistive losses occur elsewhere in the system.

A voltage loss of 62 mV in the FTO is not negligible and mitigation of this loss would still be useful, especially when the area of the photoanode is increased beyond 50 cm^2 and higher photocurrent densities are considered. Our calculations fall in line with what has been previously reported for the resistive losses caused by large area FTO substrates.[36] This problem has also been encountered in photovoltaic cells, where the sheet resistance of FTO used as a top contact layer is too high for efficient current collection.[37] This is typically resolved by depositing highly conductive metallic busbars on the front contact of the PV cells. Since these metallic busbars partially block light from reaching the PV junction, a tradeoff has to be made between optical exposure and current collection by optimizing the thickness, spacing, and pattern of the grid lines. Taking the same approach as in photovoltaics, we investigated the deposition of conductive lines to overcome the ohmic losses in the substrate. The maximum potential drop in the middle between two metallic lines, V_{drop}, is a function of the FTO sheet resistance, R_{sh}, the photocurrent density, J_{photo}, and the distance between metallic lines, w, and can be estimated using eqn (1).

$$V_{drop} = \frac{1}{8} R_{sh} J_{photo} w^2 \tag{1}$$

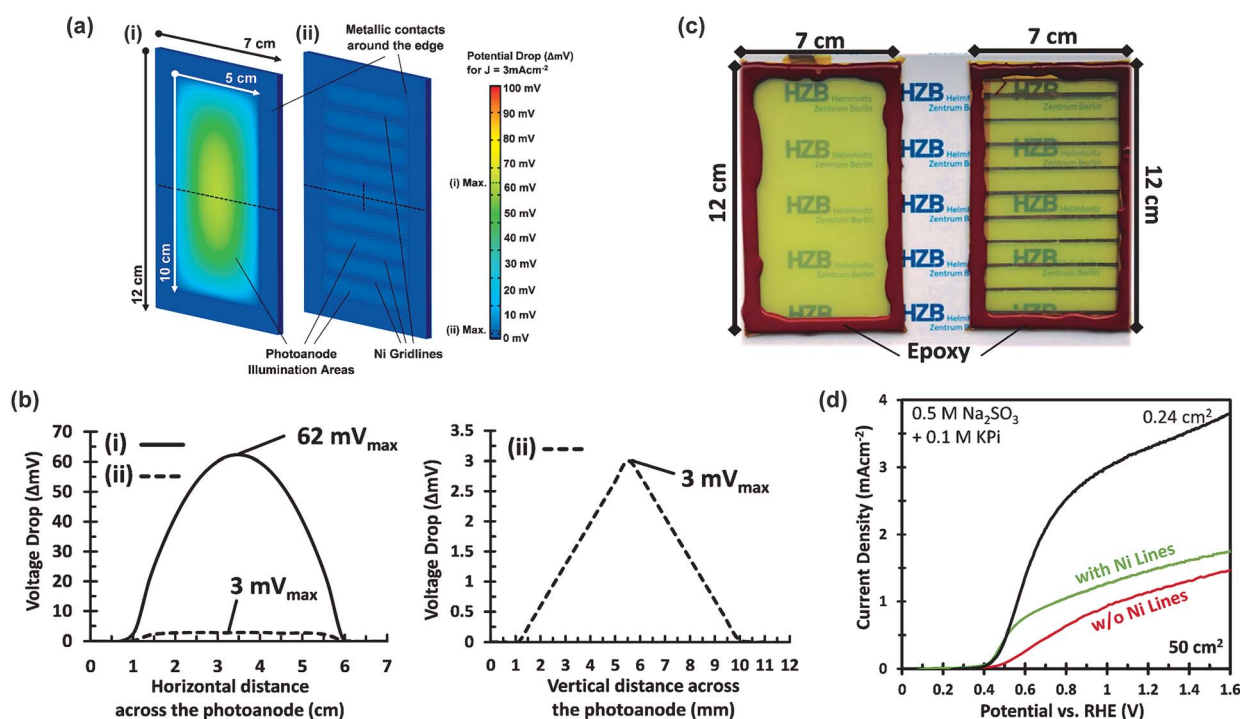**Fig. 3** (a) Colour gradient plots of the simulated potential distribution across a 5 $\times$ 10 cm^2 photoanode (i) without and (ii) with Ni lines for a photocurrent density of 3 mA cm^{-2}, and (b) shows the graphical plots of the potential drop at different points across the photoanodes (dashed lines in Fig. 3a). (c) Photographs of two 50 cm^2 area W:BiVO$_4$ photo-anodes, (i) without and (ii) with Ni lines. (d) *J*−*V* curves of the corresponding photoanodes in an electrolyte containing 0.5 M Na$_2$SO$_3$ and 0.1 M KP$_i$ buffer of pH 7, with backside AM1.5G illumination (BSI).

This equation, which is derived in ESI Note S3,† assumes that the generated photocurrent density is the same everywhere and that edge effects can be ignored. Calculated values of the potential drop for different line spacings and current densities are shown in Fig. S5.† To limit the potential drop to <5 mV at photocurrent density of 3 mA cm^{-2}, the metallic lines need to be separated by about 1 cm. We have also simulated the distribution of this potential drop using the DC conductivity model (Fig. 3a and b). Indeed, the addition of metallic lines spaced 0.9 cm apart results in a maximum potential drop of only ~3 mV at 3 mA cm^{-2}.

Based on these calculations, 200–300 nm thick Ni lines with a 2 mm width and a spacing of 9 mm were electrodeposited onto the FTO substrates prior to deposition of the W:BiVO$_4$ layer (Fig. 3c). The resistance of the Ni lines, measured over a distance of 2 cm, is *ca.* 1.5 Ω and did not change significantly after annealing at 450 °C (Fig. S6†). As shown in Fig. 3d, a significant improvement is observed at low photocurrents, just above the onset potential. At photocurrents beyond 0.8 mA cm^{-2} the improvement becomes less pronounced, which suggests that another process becomes performance-limiting at these current densities (see section 2.2). The Ni lines improve the average AM1.5G photocurrent by *ca.* 30% to 1.5 mA cm^{-2} at 1.23 V$_{RHE}$. Despite this improvement, the photocurrent is still a factor of 2 below the photocurrent density for the small area sample. It is important to consider that under back side illumination, the Ni lines block light from reaching the W:BiVO$_4$ layer. This effectively renders the area covered by the Ni lines inactive. For an average sample, we deposited 9 Ni lines (~0.2 × 5 cm^2 each) within the active area of the photoanode, which decreases the total active area from 50 cm^2 to 41 cm^2. Note, however, that we always use a value of 50 cm^2 for calculating the photocurrent density. This corresponds to the 'designated illumination area'.[38] The reported values are thus conservative, and can be significantly improved by optimizing the geometry of the Ni lines. This is, however, beyond the scope of this study.

1.2 Film quality and uniformity. Other possible causes for a decrease in photocurrent density when scaling up the photo-electrode area are the quality and uniformity of the W:BiVO$_4$ thin films. To ensure a homogeneous thickness over a larger deposition area with a single spray nozzle, we used a higher spray rate than for the small area samples (see Experimental procedures and Fig. S7†). X-ray diffraction analysis shows that the monoclinic scheelite phase is present in the large and small area samples (Fig. S8†). To investigate if the photoactivity of the film is also homogeneous, we cut two small pieces (1 × 2 cm^2) from a 50 cm^2 W:BiVO$_4$ photoelectrode: one from the center and another from the edge. We observe no apparent thickness difference between the BiVO$_4$ layer at the center and edge; scanning electron microscopy (SEM) shows that the film thickness is ~200 nm (Fig. S9†), which is consistent with our previous reports on small area W:BiVO$_4$.[6,39] The photo-electrochemical performance of these two pieces (measured with an illuminated area of 0.24 cm^2) is the same and nearly identical to that of the original small area W:BiVO$_4$ electrodes (see Fig. 1). We therefore conclude that the quality of the deposited film is uniform for samples up to 50 cm^2 in size, and

that this is not the cause of the discrepancy between the small and large area samples.

To investigate whether the uniformity of the large area W:BiVO$_4$ photoanodes is affected by the deposition of Ni lines, different parts of the electrode were masked. As shown in Fig. 4, the 5 × 10 cm^2 samples were divided into four equal parts of 12.5 cm^2 each. The AM1.5G photocurrents of each part are shown in Fig. 4, and the variation between the samples remains minimal (less than ±13%). Interestingly, even with a smaller illumination area (12.5 cm^2) the measured photocurrent density is still close to 1.5 mA cm^{-2}, matching that of the large area under full illumination (50 cm^2). This implies that other factors not yet considered limit the photocurrent density, which will be discussed in the next section.

2. PEC performance of 50 cm^2 BiVO$_4$ photoanode for water oxidation

One major difference between the measurements for the small and large area samples is the size of the photoelectrochemical cell used. The larger volume may lead to higher ohmic losses in the electrolyte and less efficient transport of the ionic species relevant for the oxygen evolution reaction (*i.e.*, H$^+$ or OH$^-$). To investigate this, the photoanodes in this section are modified with CoP$_i$ and measured in a 2.0 M KP$_i$ buffer (without hole scavenger) in order to ensure efficient charge transfer and fast water oxidation kinetics.[6,39–41]

2.1 Uniformity of large area cobalt phosphate (CoP$_i$) deposition. As shown in Fig. 5a, without hole scavenger and without CoP$_i$ surface modification, the photocurrent density at 1.23 V$_{RHE}$ is less than 0.5 mA cm^{-2} (orange curve), since the large area W:BiVO$_4$ is severely limited by surface recombination.[40] It should be noted that 2 M KP$_i$ buffer concentration was used in order to avoid ionic conductivity limitations (*vide infra*). CoP$_i$ deposition onto the W:BiVO$_4$ surface was able to suppress this recombination and enhance the photocurrent (green curve), consistent with our previous report for small-area W:BiVO$_4$.[6] At sufficiently positive potentials the photocurrent approaches the hole scavenger photocurrent (blue curve); the discrepancy at modest applied potentials is due to moderate charge injection
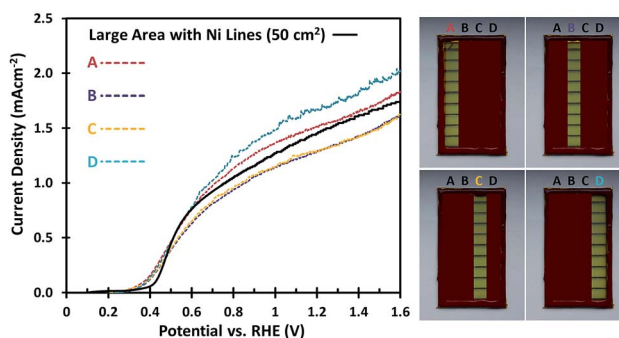

Fig. 4 AM1.5G *J*–*V* curves for the W:BiVO$_4$ photoanodes with Ni lines, measured on 4 different areas of the sample (right, A–D) to determine the uniformity of the photocurrent across the large area sample, with an electrolyte containing 0.5 M Na$_2$SO$_3$ and 0.1 M KP$_i$ buffer of pH 7.
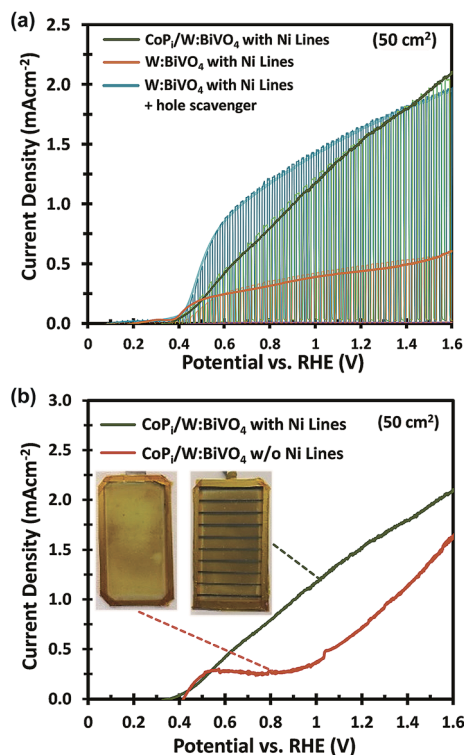
Fig. 5 (a) J–V curves under constant, dark and chopped AM 1.5G illumination comparing the performance of large area (50 cm²) W:BiVO₄ photoanodes with Ni lines, either in 2.0 M KPᵢ buffer solution with 0.5 M Na₂SO₃ (blue), or without hole scavenger, before (orange) and after (green) photo-electrodeposition of CoPᵢ. (b) J–V curves comparing CoPᵢ-modified W:BiVO₄ photoanodes with (green) and without (red) Ni lines measured in 2.0 M KPᵢ buffer, pH 7, under AM 1.5G illumination. Inset: photographs of the CoPᵢ deposited on W:BiVO₄ photoanodes without (left) and with (right) Ni lines.

efficiency.[6,7] A photocurrent density of 1.5 mA cm⁻² at 1.23 V$_{RHE}$ was achieved for water oxidation with 50 cm² CoPᵢ-modified W:BiVO₄ electrodes.

The importance of the Ni lines during the photo-electrodeposition of CoPᵢ is illustrated in Fig. 5b. Without Ni lines, we obtained a rather poor coverage quality of CoPᵢ (see inset of Fig. 5b), which subsequently results in a poor water oxidation performance. The coverage of CoPᵢ is very much improved with Ni lines. We speculate that the improved homogeneity of CoPᵢ is arising from the uniformity of the potential drop across the substrates with Ni Lines. At the initial stage of CoPᵢ photo-electrochemical deposition, we observe a large spike in the anodic photocurrent density for all samples, as is typical for photoelectrodeposition of CoPᵢ.[42,43] This initial photocurrent contributes significantly to the nucleation and growth of CoPᵢ. As confirmed in Fig. 3a and b, at relatively high current densities (>3 mA cm⁻²), a potential drop >70 mV can be expected within the central region of the samples without Ni lines. Such a potential drop could inhibit CoPᵢ nucleation and therefore lead to the non-uniform deposition of CoPᵢ in these large area samples. Interestingly, the distribution of CoPᵢ deposited on the samples without Ni lines (inset of Fig. 5b) closely resembles the color gradient plots of the potential

distribution across a 5 × 10 cm² photoanode without Ni lines (see Fig. 3a). We therefore conclude that the combination of (i) applying Ni lines to the FTO substrate and (ii) photo-electrodeposition of CoPᵢ is essential to improve the photocurrent of large area W:BiVO₄ photoanodes for water oxidation.

2.2 Electrolyte conductivity limitations. Another possible scale-up limitation that we have already briefly alluded to is the electrolyte conductivity. For PEC water oxidation with BiVO₄, a KPᵢ buffer (pH 7) electrolyte is commonly used. This serves as the supporting electrolyte to ensure a sufficiently high conductivity, but it also serves to stabilize the pH of electrolyte and maintain the stability of the CoPᵢ overlayer.[44] A KPᵢ concentration of 0.1 M is typically used for PEC measurements of small area BiVO₄ electrodes by our group and others;[4,5,7,15] this concentration was also initially used for our large area electrodes. However, while such a low concentration may provide enough ionic conductivity for a small area electrode configuration, it may not be enough for a large area electrode. This is simply caused by the fact that the distance between electrodes in a large area configuration (up to 6 cm in our large area PEC cell) is much greater than that in a small area configuration (<1 cm).

To better understand the role of electrolyte conductivity, we first measured the specific conductivities for a series of KPᵢ electrolytes at pH 7 as a function of concentration (Fig. S10†). The conductivity values in Fig. S10† are consistent with previously reported values for these electrolytes.[45] The electrolyte conductivity shows a non-linear increase with electrolyte concentration, especially at higher concentration. The non-linearity is caused by the increasing interaction between the ions, resulting in a decrease in molar conductivity with increasing concentration.[46]

Fig. 6 shows the photocurrent measured at 1.23 V$_{RHE}$ as a function of electrolyte concentration for the small and large area CoPᵢ/W:BiVO₄ photoanodes, normalized to the photocurrent measured in 0.1 M KPᵢ. For the small area electrode, it is

Fig. 6 Normalized photocurrent measured at 1.23 V$_{RHE}$, under AM 1.5G illumination, for the small and large CoPᵢ/W:BiVO₄ photoanodes as a function of concentration of electrolyte (pH 7). Zero concentration corresponds to pure deionized water. *Electrolyte selected for all measurements using the large area BVO₄ without hole scavenger.

clear that KP_i concentrations from 0.1 M to 2.0 M have no effect on the overall photocurrent. This indicates that a 0.1 M KP_i buffer solution provides sufficient ionic conductivity for small area PEC cells (<1 cm^2), even at neutral pH. For the large area electrode, on the other hand, the photocurrent is found to increase with increasing electrolyte concentration. This correlation is not specific to phosphate buffer, since a similar dependence was also observed when measurements were performed in sodium sulfate (Na_2SO_4) electrolyte (see Fig. 6). In KP_i buffer, the photocurrent can be improved by 40% by simply increasing the KP_i concentration from 0.1 M to 2.0 M. Concentrations of KP_i greater than 2.0 M were not used in this investigation, since the saturated solution would rapidly precipitate on the walls of the cell and bubbles would begin to stick to the electrodes.

Using the measured electrolyte conductivity of the KP_i buffer, the potential drop between a 50 cm^2 $BiVO_4$ photoanode and the Pt counter electrode can be estimated using a simple iR model. The average distance between the working and counter electrodes in our large area PEC cell, shown in Fig. S11,† is estimated to be 3 cm. This leads to an overall potential drop across the electrolyte of $ca.$ 600 mV for a 0.1 M KP_i solution (15 mS cm^{-1}) and a photocurrent density of 3 mA cm^{-2}. In contrast, when a 2 M KP_i solution is used with a conductivity of 130 mS cm^{-1}, the potential drop decreases by almost an order of magnitude to $ca.$ 69 mV. Despite the improvements by the deposition of Ni lines and increasing the electrolyte concentration, the photocurrent of the large area W:$BiVO_4$ (1.5 mA cm^{-2} at 1.23 V_{RHE}) is still well below its small area equivalent. Our calculations indicate that the remaining ohmic losses for photoanodes with Ni lines in 2 M KP_i electrolyte would amount to approximately $3 + 69 = 72$ mV for a photocurrent density of 3 mA cm^{-2}; this voltage drop cannot explain the photocurrent difference between the small and large area electrode. Instead, we tentatively attribute this discrepancy to the low concentration ($\sim 10^{-7}$ M) of H^+/OH^- species at neutral pH. At such low concentrations, diffusion of these species cannot keep up with the rate at which they are generated (H^+) and consumed (OH^-), resulting in local enhancement and depletion, respectively, of these species. This results in a local decrease of the pH near the photoanode surface and a corresponding positive shift of the Nernst potential of the oxygen evolution reaction that will lead to a decrease in photocurrent. We note that in the KP_i buffer electrolyte, due to the low concentration of OH^-, the actual species that is oxidized is water,[47] resulting in the formation of protons that have to diffuse away from the surface. Moreover, the transport of H^+/OH^- is essentially governed by the movement of buffer components ($i.e.$, the $H_2PO_4^-$ and HPO_4^{2-} ions); the term "effective H^+/OH^- conductivity" would therefore be more appropriate here.

To further confirm that H^+/OH^- transport limits the performance, we performed two-electrode electrochemical water splitting experiments in the dark. We used two sets of identical Pt-coated FTO electrodes, one set with a surface area of 0.24 cm^2 for each electrode, and one set with a 40 cm^2 electrode area. The large-area FTO/Ag/Pt electrodes are highly conducting, with a resistivity that is $ca.$ 60 times smaller than that of

bare FTO (Fig. S12†). The two electrodes in each set are placed in a large beaker and are oriented parallel to each other, separated by a distance of 2 cm (see Fig. 7a and S13†). For each set of electrodes, we measured the J–V curves in 2.0 M KP_i (pH 7) and in 0.6 M KOH (pH 13). The KOH concentration was chosen to ensure that the total electrolyte conductivity is the same as that of the 2.0 M KP_i (130 mS cm^{-1}). The results are shown in Fig. 7a. For the large-area electrodes, the pH 7 electrolyte (solid red curve) requires much higher overvoltages than the pH 13 solution (dashed red curve). Using eqn (1), the voltage drop within the FTO/Ag/Pt electrodes is calculated to be less than 23 mV for a current density of 10 mA cm^{-2}. This shows that most of the voltage drop occurs in the electrolyte. This is indeed consistent with hypothesis that a low concentration of H^+/OH^- limits the water splitting current.
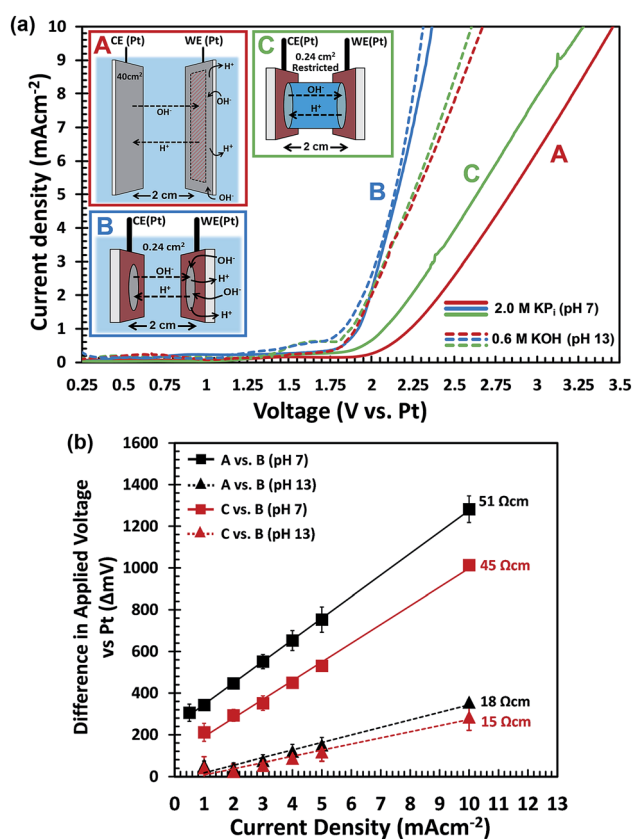

Fig. 7 (a) Voltammograms for water splitting in a two-electrode setup, using two identical Pt electrodes in three different configurations (A–C) and in two different electrolytes: 2.0 M KP_i, pH 7 (solid curves) and 0.6 M KOH, pH 13 (dashed curves) using a scan rate of 10 mV s^{-1}. The inset shows the three different cell configurations in which the two Pt electrodes are oriented parallel to each other and separated by 2 cm. A: large area Pt electrodes in a large electrolyte volume, B: small area Pt electrodes in a large electrolyte volume and C: small area Pt electrodes in a restricted cell volume. (b) Additional overvoltages needed to achieve a certain current density for (black squares) (A) $vs.$ (B) in 2.0 M KP_i (pH 7), (black triangles) (A) $vs.$ (B) in 0.6 M KOH (pH 13), (red squares) (C) $vs.$ (B) in 2.0 M KP_i (pH 7), and (red triangles) (C) $vs.$ (B) in 0.6 M KOH (pH 13). Data points follow a linear fit and error bars indicate standard deviations of 5 repeated measurements. The resistivities (in Ω cm) were calculated from the slopes of the curves divided by the distance between the electrodes (2 cm).

For the small-area electrode, the results seem counter-intuitive at first; the J–V curves almost overlap for the pH 7 and pH 13 solutions (solid and dashed blue curves, respectively). This can, however, be understood when realizing that the radius of the electrodes ($\sim$0.3 cm) is much smaller than the distance between them (2 cm). This means that for the pH 7 measurement, the OH^- species can be replenished from the surrounding electrolyte,[48,49] *i.e.*, the bulk electrolyte volume beyond the cylindrical volume between both electrodes (Fig. S13B†). To verify this, we constructed a cell in which the electrolyte was restricted to the cylindrical volume between the two small-area electrodes (Fig. S13C†). The resulting J–V curves for the 'restricted' configuration are shown in green in Fig. 7a. In contrast to the 'unrestricted' configuration, the J–V curve recorded in the pH-neutral KP_i electrolyte (solid green curve) shows a much larger overvoltage than the measurement in 0.6 M KOH (dashed green curve). The pronounced differences between the restricted and unrestricted curves provides direct evidence that diffusion of OH^- species from the surrounding electrolyte mitigates the depletion of OH^- species and leads to a reduction in the required overvoltage.

It should be noted that even at pH 13, the restricted configuration (dashed green curve) shows a few tenths of a volt more overvoltage than the unrestricted configuration (dashed blue curve). This indicates that even at these high pH values and relatively modest current densities, depletion of OH^- can become an issue. While further increase of the pH will help to mitigate this, it may also lead to corrosion of the (photo)electrode. A better strategy would be to decrease the distance between the electrodes and/or to reduce the electrode area-to-electrolyte volume ratio in order to facilitate the replenishment of OH^- from the surrounding electrolyte.

To visualize the data from Fig. 7a in a different manner, we plotted the differences in required overvoltages under various conditions as a function of current density (Fig. 7b). The black curves show the additional overvoltage needed when scaling a small area electrode to a large area at pH 7 and at pH 13. The difference in slopes show that the resistive losses for scale-up to 50 cm^2 are $\sim$3 times higher at pH 7 than at pH 13, despite the fact that both electrolytes have the same total ionic conductivity (130 mS cm^{-1}). The red curves show the additional overvoltage needed when 'restricting' the electrolyte volume around a small area electrode at pH 7 and at pH 13. The difference in slope for both pH values is again a factor of 3. The perfectly linear slopes of all curves in Fig. 7b confirm that the voltage losses due to scale-up and restriction of the electrolyte volume are purely resistive in nature. This is consistent with the notion that these losses are due to mass transport limitations of OH^-. One unexpected observation is that not all curves in Fig. 7b go exactly through the origin, which is what one would expect for purely resistive losses. We attribute this to slight variations in the concentration of dissolved oxygen gas during the experiments. This induces Nernstian shifts in the potentials of the electrochemical half-reaction which affects the onset potential of the current–voltage curves.

Interestingly, the additional resistivity introduced by restricting the electrolyte volume in a small area cell at pH 13 is comparable to the resistivity introduced by scale-up of this same cell from 0.24 cm^2 to 50 cm^2 at the same pH (red *vs.* black triangles in Fig. 7b). This clearly shows that diffusion (or lack thereof) of OH^- species from the surrounding electrolyte can have a profound influence on the resistive losses in the system.

These results again show that the depletion of H^+/OH^- at the surface of the electrodes—as a result of the low initial concentration (neutral pH) and restricted diffusion from the surrounding electrolyte—is the main cause of efficiency losses when scaling up small area electrodes. A possible engineering approach to avoid such limitations is to divide a single large-area electrode into multiple segments in order to optimize flow patterns and avoid undesired pathways for ionic species.[50,51]

Finally, although not demonstrated here, we note that the moderate electrolyte conductivity may also result in a spatial distribution of the surface potential across the large area $BiVO_4$ photoanodes, known to further limit the PEC performance of large area photoelectrodes. Hankin *et al.* recently reported that without an appropriate electrode configuration and electrolyte conductivity, a 10×10 cm^2 hematite (α-Fe_2O_3) photoanode would exhibit inhomogeneous spatial distribution of surface potentials and current densities. This would be detrimental to the resultant hydrogen/oxygen evolution efficiencies. It was also stated that for α-Fe_2O_3 photoanodes with an area of 10×10 cm^2, an electrolyte concentration in excess of $\geq$1 M KOH would be required.[28]

3. Unassisted PEC–PV water splitting devices

In the previous sections we have outlined our efforts to improve the PEC performance of large area W:$BiVO_4$ photoanodes and minimize the discrepancy with the small area samples. The next step is to integrate these large-area photoanodes into complete PEC–PV water splitting devices.

The W:$BiVO_4$ photoanodes was placed in front of series-connected silicon heterojunction (SHJ) solar cells (positioned side-by-side), each with an area of 25 cm^2. In this stacked configuration, the light interacts with the different device components in the following order upon entering: glass/FTO/$BiVO_4$/CoP_i/electrolyte/glass/SHJ. The advantage of this configuration is that the $BiVO_4$ electrode is illuminated *via* the back side, which gives higher photocurrents than front-side illumination.[6,52,53]

Furthermore, the Pt mesh counter electrodes were placed at both sides of the photoanodes outside of the light path and were connected to the n-terminal of the SHJ solar cells. The two-electrode J–V curves of the 50 cm^2 CoP_i/W:$BiVO_4$ photoanode and of the series-connected SHJ cells (placed behind the $BiVO_4$ electrode) are shown in Fig. 8a. From the intercept of these individual curves, an operating photocurrent of 1.5 mA cm^{-2} at *ca.* 1.23 V is expected. Indeed, the measured short-circuit photocurrent density (at zero bias) of the integrated device is *ca.* 1.5 mA cm^{-2}, as shown in Fig. 8b. This corresponds to an STH efficiency of 1.9%.

Our PEC cell configuration also allows for the use of two stacked $BiVO_4$ photoanodes in conjunction with the PV cells. In
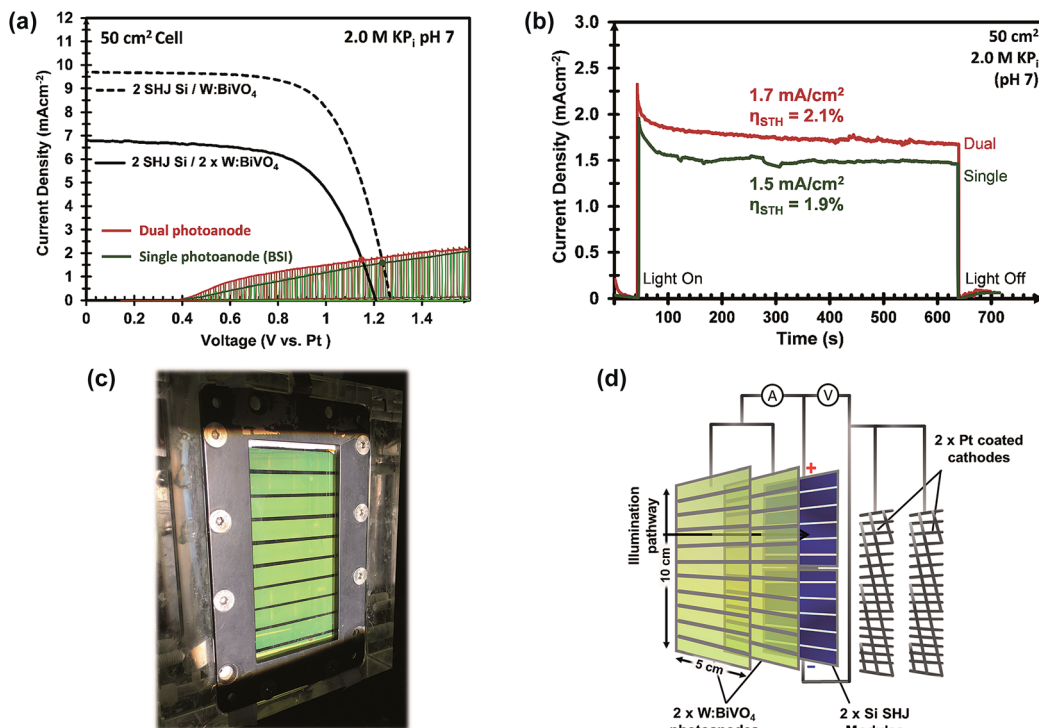
Fig. 8 (a) $J-V$ curves for the 50 cm^2 2× SHJ PV module behind single (dashed black lines) or dual (solid black lines) W:BiVO$_4$ photoanodes, and $J-V$ curves for the 50 cm^2 single (green) and dual (red) W:BiVO$_4$/CoP$_i$ photoanodes under chopped AM 1.5G illumination. (b) Current density and voltage *vs.* time for the 50 cm^2 PEC–PV devices with single (green) and dual (red) photoanode configurations over 10 min. All measurements were conducted in a stirred 2.0 M KP$_i$ electrolyte at pH 7. (c) Photograph of the large area (50 cm^2) integrated PEC–PV device in the dual photoanode configuration with a device structure of W:BiVO$_4$(BSI)/Electrolyte/W:BiVO$_4$(FSI)/2SHJ-PV/2Pt, illustrated in (d). BSI: back-side illuminated, FSI: front-side illuminated.

this so-called "dual photoanode" configuration the total amount of light absorbed by the BiVO$_4$ is distributed over two photoanodes, which offers a solution for the usual trade-off between optical absorption and carrier diffusion length in metal oxide photoelectrodes.[15] As shown in Fig. 8c and d, the PEC–PV cell employs the first CoP$_i$/W:BiVO$_4$ layer as the front window of the cell (back-side illuminated, BSI), and the second CoP$_i$/W:BiVO$_4$ layer as its back window (front-side illuminated, FSI), with the Si solar cells also attached to this back window. The second BiVO$_4$ photoanode provides an additional photocurrent of 0.21 mA cm^{-2} at 1.23 V$_{RHE}$, which originates from the remaining supra-bandgap photons that were not absorbed by the first W:BiVO$_4$ photoanode. The two-electrode $J-V$ curve of

the dual CoP$_i$/W:BiVO$_4$ photoanode is also shown in Fig. 8a (red curve); a *ca.* 10% improvement is obtained by the dual photoanode configuration. This results in an average operating photocurrent density of *ca.* 1.72 mA cm^{-2} (Fig. 8b). This corresponds to an STH efficiency of 2.1%, which, to the best of our knowledge, represents a new performance record for a large area (>10 cm^2) solar water splitting PEC–PV device based on metal oxide photoelectrodes.

To illustrate the significance of the BiVO$_4$ photoanodes to the overall device performance, a cell consisting of a Pt cathode/ 2 series-connected SHJ/Pt anode was also tested. Upon direct illumination to the SHJ cells, only a negligible photocurrent and STH efficiency (<0.1%) was achieved. Table 2 summarizes the

Table 2 Summary of the performance characteristics for the small (0.24 cm^2) and large (50 cm^2) area PEC–PV devices under AM 1.5G illumination. 0.1 M and 2.0 M KPi buffer solutions were used for the small and large area PEC–PV devices, respectively. BSI: back-side illuminated, FSI: front-side illuminated

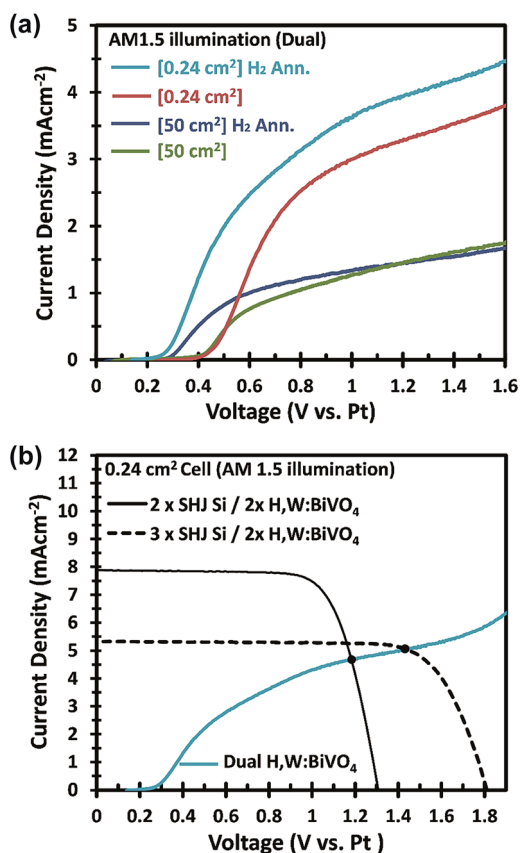| PEC–PV Configuration	Illum. Area (cm^2)	J (mAcm^{-2})	I (mA)	Average. STH Efficiency. (%)
Pt/2-SHJ/Pt	50	0.02	1.0	0.03
CoP$_i$/W:BiVO$_4$(FSI)/2-SHJ/Pt	50	1.00	50.0	1.2
CoP$_i$/W:BiVO$_4$(BSI)/2-SHJ/Pt	50	1.50	75.0	1.9
Dual-CoP$_i$/W:BiVO$_4$/2-SHJ/Pt	**50**	**1.72**	**86.0**	**2.1**
Dual-CoP$_i$/H,W:BiVO$_4$(FSI)/2-SHJ/Pt	**0.24**	**4.45**	**1.07**	**5.5**
Dual-CoP$_i$/H,W:BiVO$_4$(FSI)/3-SHJ/Pt	0.24	5.12	1.23	6.3

Fig. 9 (a) *J−V* curves comparing the effects of hydrogen annealing on the small and large area dual-CoP$_i$/W:BiVO$_4$ photoanodes in 0.1 M KP$_i$ (small area) or 2.0 M KP$_i$ (large area) buffer. Large area samples are with Ni lines. (b) *J−V* curves of a small area 2 SHJ PV (black line) and the 3 SHJ PV (dashed black line) with dual-CoP$_i$/H,W:BiVO$_4$ photoanodes as the front windows, and the small area dual-CoP$_i$/H, W:BiVO$_4$ photoanode, measured in 0.1 M KP$_i$ buffer.

key performance characteristics for the different PEC–PV configurations under AM 1.5G illumination.

Current density *vs.* time measurements (Fig. 8b) showed that both the single and dual photoanode devices displayed pronounced transients during the first 100–200 s, after which the photocurrent remains relatively stable. During these measurements the formation of bubbles at the electrodes could be clearly observed (see Video in the ESI†). The electrolyte required constant agitation with N$_2$ purging in order to release the bubbles from the surface of the electrodes and to prevent them from scattering the light away from the series-connected Si PV cells (and the second photoanode). Without this N$_2$ purging and agitation, the photocurrent drops rapidly within the first 1–2 min of operation due to rapid bubble formation that block the optical pathway to the back electrode and PV (second W:BiVO$_4$ and Si PV). These observations show that a full recirculation system is needed for long-term operation of the device. Long term stability measurements of the single and dual large area PEC–PV devices, presented in Fig. S14,† shows a turbulent (due to N$_2$ bubbling), and relatively stable photocurrent density for up to 7 hours. The total amount of photo-

generated charge that passed during these experiments exceeds the amount needed to photo-corrode the 200 nm BiVO$_4$ film by a factor of ∼110 (assuming 8 holes are needed to photo-dissolve one BiVO$_4$ unit), and exceeds the amount of charge needed to deposit the CoP$_i$ by a factor >600. This means that the faradaic efficiency is >99%.

It should be noted that the efficiencies mentioned above do not take into account chemical recombination due to crossover of oxygen to the cathode side. Since no membrane was used, crossover will indeed occur, which would lower the actual solar-to-hydrogen efficiency. However, this does not affect the STH values determined from the measured photocurrent.

In an attempt to further improve the efficiency, we used a hydrogen annealing treatment for the BiVO$_4$ photoelectrodes. We recently reported that a mild hydrogen treatment (300 °C anneal in 2.4% H$_2$/Ar for 10 minutes) effectively enhances the charge carrier lifetime in BiVO$_4$ photoanodes.[54] Applying the same hydrogen treatment to a small area W:BiVO$_4$ photoanode also results in significant improvement of the photocurrent, as shown in Fig. 9a; AM1.5G photocurrent of 4.0 mA cm^{-2} was achieved at 1.23 V$_{RHE}$ for the hydrogen-treated tungsten-doped BiVO$_4$ (H,W:BiVO$_4$). By combining two CoP$_i$/H,W:BiVO$_4$ electrodes in a dual photoanode configuration with 2 series-connected SHJ solar cells, a 0.24 cm^2 PEC–PV device with an operating photocurrent of 4.5 mA cm^{-2} is achieved (Fig. 9b). This corresponds to an STH efficiency of 5.5%, which is amongst the highest reported efficiencies for an oxide-based solar water splitting device (Table 1). Combination with three series-connected SHJ cells gave an even higher efficiency of 6.3%. It should be noted that three series-connected SHJ cells can split water even without the BiVO$_4$ photoanodes (Fig. S15†), albeit at lower efficiency (3.08 mA cm^{-2} ≈ 3.8%).

Hydrogen treatment of the large-area BiVO$_4$ photoanodes was done in a rapid thermal processing (RTP) system, since the electrodes do not fit in our regular tube furnace. Although the onset potential is shifted cathodically (see Fig. 9a), the photo-current at 1.23 V$_{RHE}$ does not improve with hydrogen treatment. Further optimization of the RTP process is needed in order to obtain the same level of improvement as for the small area BiVO$_4$ photoanodes.

Conclusions

In summary, we have demonstrated a large area (50 cm^2) PEC–PV water splitting device based on a W:BiVO$_4$ top absorber and a silicon heterojunction bottom absorber and discussed the challenges encountered during scale-up of this system. Spray pyrolysis was used to fabricate 50 cm^2 W:BiVO$_4$ photoanodes of uniform thickness and quality. However, the photo-electrochemical performance of the large area photoelectrode was significantly lower than the small area equivalent. We found that only 10% of the voltage drop in the large area system is due to ohmic losses in the FTO substrate, while using a 2.0 M instead of 0.1 M buffer concentration in the electrolyte can increase the photocurrent by up to 40%. Both of these factors do not affect the performance of the small area electrode. We mitigated these losses by depositing metallic Ni lines onto the FTO substrate prior

to the W:BiVO$_4$ deposition and by increasing the electrolyte (KP$_i$ buffer) concentration. The Ni lines significantly improved the uniformity of the electrodeposited CoP$_i$ and resulted in an AM1.5 photocurrent of ~1.5 mA cm^{-2} at 1.23 V *vs.* RHE for a 50 cm^2 CoP$_i$/W:BiVO$_4$ photoelectrode. The main bottleneck, however, is the low concentration of H$^+$/OH$^-$ reactant species in pH-neutral solutions. This leads to poor conductivity and rapid depletion of these species in the electrolyte, which causes pH changes and potential drops up to 500 mV at a current density of 3 mA cm^{-2}. Despite these losses, a STH efficiency of 2.1% was achieved for a combination of two large area CoP$_i$/W:BiVO$_4$ photoanodes in a dual photoanode configuration, connected in tandem to two series-connected SHJ solar cells. Although this efficiency is the highest reported thus far for large area (>10 cm^2) unassisted solar water splitting based on metal oxide photoelectrodes, it is still a factor of 3 lower than the 5.5% STH efficiency that we achieved in this study for the corresponding small area device. Reduction of these scale-up losses requires either strongly acidic or alkaline solutions to avoid local pH gradients, or innovative engineering solutions in the device design that allows the use of pH-neutral solutions.

Experimental

4. Masking and pre-treatment of the large area FTO substrates

Prior to electrodeposition, the 7 × 12 cm^2 TEC 7™ FTO substrates were cleaned thoroughly with soapy water (10 vol% Triton-X™), ethanol, and then dried under a flow of compressed N$_2$. The substrates were then masked with Kapton® tape for the deposition of 7 cm long, 2 mm wide conducting Ni lines. The lines were separated by the width of the tape (0.9 cm). To improve the adhesion of the electrodeposited Ni lines, the masked FTO substrates were treated with a chemical reduction process, described in more detail elsewhere.[55,56] Briefly, masked FTO substrates were immersed in 1.0 M glycine (≥99%; Aldrich), 0.5 M FeSO$_4$·7H$_2$O (≥99%; Aldrich) in deionized water was adjusted to a pH ~2.5 using H$_2$SO$_4$ and NaOH. The masked FTO substrates were immersed in the solution horizontally for 3 min (FTO-side facing upwards). Zn powders (mesh 100) were then uniformly dispersed over the FTO and allowed to settle on the surface for 10 min, during which hydrogen bubbles evolved. The substrates were then removed and washed with a fast jet of deionized water. This resulted in the formation of a shiny adherent intermetallic film consisting of Fe$_x$Sn$_y$ on the surface of the unmasked regions of the FTO.

5. Electrodeposition of Ni lines

The electrochemical deposition of Ni lines was performed in a three-electrode electrochemical cell using a VersaSTAT 3 potentiostat/galvanostat (Ametek). The pre-treated masked FTO acted as the working electrode and a Pt wire served as the counter electrode. An Ag/AgCl reference electrode was used (XR300, saturated KCl, Radiometer Analytical). Ni was electrochemically deposited under galvanostatic conditions at a current density of −5 mA cm^{-2} (an absolute current of −50 mA for our typical

masked FTO sample) for 900 s. The electrochemical bath was composed of 1.14 M NiSO$_4$·7H$_2$O (≥98%, Aldrich), 0.16 M NiCl$_2$·6H$_2$O (≥98%, Aldrich), and 0.73 M H$_3$BO$_3$ (≥99.5%, Aldrich) in deionized water (>18 MΩ cm). The bath was heated to 50 °C and stirred during the electrochemical deposition. After the deposition, the Kapton tape was removed and the FTO with Ni lines were ultrasonically cleaned in deionized water, acetone, and ethanol, each for 60 s, then dried under a fast jet of N$_2$.

6. Fabrication of W-doped BiVO$_4$ photoanodes

First, a ~10 nm thick tin oxide (SnO$_2$) layer was deposited onto cleaned FTO substrates (with or without Ni lines) by spray pyrolysis using a solution of 0.1 M SnCl$_4$ in ethyl-acetate. The substrate temperature was 450 °C. Subsequently, ~200 nm thick BiVO$_4$ photoanodes with 1% W doping were deposited by spray pyrolysis using a previously reported precursor solution consisting of 4.44 mM Bi(NO$_3$)$_3$·5H$_2$O (98%, Sigma-Aldrich), 4.44 mM VO(C$_2$H$_7$O$_2$)$_2$ (99%, Alfa Aesar) and 0.044 mM W(C$_2$H$_5$O)$_6$ from 5% w/v in ethanol (99.8%, Alfa Aesar).[6] The solvent consists of a 10 vol% of acetic acid in absolute ethanol. For the fabrication of 0.24 cm^2 photoanodes a spray rate of 1–1.5 mL per spray cycle was used. For the 50 cm^2 photoanodes, the spray rate was adjusted to 2–2.5 mL per spray cycle by increasing the carrier gas pressure. The increase in spray rate enlarged the area covered by the mist generated by the spray nozzle, and ensured a homogeneous deposition over larger areas (Fig. S7†). Each spray cycle consisted of 5 s of spraying, followed by a 55 s of pause to allow solvent evaporation. This cycle was repeated 180 times using a home built automatic spray controller. The overall volume of precursor used was ~180 mL for a 0.24 cm^2 sample and ~360 mL for a 50 cm^2 sample. Special precautions had to be taken to prevent cracking and damage to the large area substrates. Specifically, the substrates were heated to 450 °C at a slow ramp rate of 5 °C min^{-1}. Furthermore, droplet formation around the edge of the substrate was a major cause of large area substrate breakage/cracking and this could be avoided by positioning the nozzle 20 cm above the substrate. After deposition the samples were cooled gradually to room temperature by turning off the heater plate, followed by annealing in air (box furnace) for 2 hours at 460 °C, using a heating rate of 5 °C min^{-1}.

7 Hydrogen annealing of W:BiVO$_4$ photoanodes

The small area W:BiVO$_4$ photoanodes were annealed in hydrogen at 300 °C for 10 minutes to improve the carrier lifetime.[54] This was done by flowing a mixture of 2.4% H$_2$/97.6% Ar (Arcal10, Air Liquide) into a tube furnace using a flow rate of 100 cm^3 (STP) min^{-1}. A heating ramp rate of 5 °C min^{-1} was used. The large area W:BiVO$_4$ photoanodes were annealed using an AS-One 100 Annealsys rapid thermal processor (RTP) using the same conditions.

8 Encapsulation of large area photoanodes

To make electrical contacts to the 50 cm^2 BiVO$_4$ photoanodes the edge of the samples were etched with conc. HCl to expose the underlying FTO. Ag paste was then applied to the exposed FTO and contacted with copper tape. The edges of the

photoanodes were sealed with RTV-1 silicone rubber (Scrintec®), to prevent cracking of the glass substrate and leakage of electrolyte.

9 Photoelectrochemical deposition of CoP$_i$ onto BiVO$_4$

The CoP$_i$ layer was deposited photoelectrochemically onto BiVO$_4$ substrates under AM1.5G illumination at a constant applied potential of +1.0 V *vs.* RHE in an electrolyte of 1.0 mM Co(NO$_3$)$_2$·6H$_2$O (≥98%, Aldrich) and 2.0 M potassium phosphate (KP$_i$) buffer with a pH of 7. The average amount of total charge passed during the deposition was ~50 mC cm^{-2} (with an illumination/deposition time of 5 min). The CoP$_i$ was subsequently conditioned by performing cyclic voltammetry in 0.1 M KP$_i$ (small area) or 2.0 M KP$_i$ (large area) buffer solution. A total of 10 cycles were performed at potentials between 0.2–1.7 V$_{RHE}$ with a scan rate of 10 mV s^{-1}, 5 dark and 5 under illumination.

10 Fabrication of FTO/Ag/Pt electrodes

Prior to electrodeposition, two 3.2 × 12.5 cm^2 and two 3.2 × 7 cm^2 TEC 7™ substrates (F-doped SnO$_2$, sheet resistance of ~7 Ω sq^{-1}, Sigma Aldrich) were cleaned thoroughly with soapy water, ethanol, and then dried under a flow of compressed N$_2$. To improve the adhesion of the electrodeposited metal films (*i.e.*, Ag, Pt), the masked FTO substrates were treated with the chemical reduction process mentioned above in order to obtain an intermetallic Fe$_x$Sn$_y$ film.

The consecutive electrochemical deposition of Ag (2 µm) and Pt (~5 nm) films onto FTO was performed with the same setup as used for the deposition of the Ni lines (*vide supra*). Ag was electrochemically deposited under galvanostatic conditions with a current density of −5 mA cm^{-2} for 1200 s. The electrolyte for the electrochemical bath was purchased from a commercial supplier (Wilaplat) and consisted of 30 gL^{-1} of Ag, and 120 gL^{-1} of cyanide salts. The bath was heated to 40 °C and stirred during the electrochemical deposition. After Ag electrodeposition, samples were cleaned with deionized water and transferred to a second electrochemical bath consisting of H$_2$PtCl$_6$ (1 gL^{-1}) and HCl (0.1 M). Pt was electrochemically deposited under galvanostatic conditions with a current density of −1 mA cm^{-2} for 600 s, resulting in the final electrode structure of SiO$_2$/FTO/Ag/Pt (Fig. S16†). The large area Pt electrodes were then cleaned with deionised water. Small area electrodes (0.24 cm^2) were fabricated by cutting the 3.2 × 7 cm^2 FTO/Ag/Pt samples into smaller segments, sealing with Scrintec® RTV-1K Silicone Rubber and creating an exposed electrocatalytic area with a 5.5 mm-diameter rubber O-ring. To restrict the electrolyte volume to the exposed area of the electrodes (Fig. S13D†), a 2 cm long polypropylene pipe with a 5.5 mm inner diameter was attached to two small electrodes using the Scrintec® Silicone Rubber. Three 2.5 mm diameter holes were made through the tube walls at both ends and the middle for gas/electrolyte removal and electrolyte inlet, respectively (see Fig. S13D†).

11 *I–V* measurements of 2× FTO/Ag/Pt electrodes

The electro-catalytic properties of the FTO/Ag/Pt electrodes with different areas (0.24 cm^2 or 40 cm^2) were measured using a two-electrode set-up. An FTO/Ag/Pt sample acted as the counter electrode and the other FTO/Ag/Pt sample as the working electrode. The electrodes were positioned precisely parallel to each other at a distance of 2 cm. In the so-called 'un-restricted' cell (Fig. S13B†), Pt electrodes were immersed in a 1.5 L volume of either 2.0 M KP$_i$, pH 7 or 0.6 M KOH, pH ~13 electrolyte. In both cases, the electrolyte conductivity was the same, *i.e.*, 130 mS cm^{-1} at 25 °C. For the small area (0.24 cm^2) 'restricted' cell (Fig. S13C†) *ca.* 1 mL of electrolyte was used. Prior to measurements, the samples were conditioned by performing 10 *J–V* cycles from −0.3 to +3.0 V *vs.* Pt with a scan rate of 10 mV s^{-1}. Measurements of the I-V curves were conducted from −0.1 to +3.5 V *vs.* Pt with a scan rate of 10 mV s^{-1}. To validate the reproducibility of these data, the measurements were repeated 5 times.

12 Fabrication, encapsulation and characterization of the PV modules

To prepare interconnected PV modules, silicon heterojunction (SHJ) solar cells were processed at PVcomB. First, wet-chemically textured (KOH) and RCA-cleaned Cz–Si wafers were laser-cut into 1 × 1 cm^2 or 5 × 5 cm^2 pieces and, subsequently, RCA-cleaned again. They were then processed by the following steps: (1) plasma enhanced chemical vapor deposition of i/p and i/n amorphous silicon thin films on each side of the n-type wafer to form hole and electron selective contacts, respectively, (2) sputter deposition of the front and rear TCO (ITO), and (3) screen printing of silver contact gridlines onto the TCO. The grid dimensions were optimized for the relatively modest (compared to normal PV operation) current densities expected for a PEC–PV tandem configuration with a BiVO$_4$ top absorber. Mini modules were then fabricated from two or three cells, flipped in polarity and glued on a metal coated glass substrates using conductive adhesive to interconnect the cells. Low-temperature soldering of connectors onto the Ag grid was done for the front contacts. Finally, encapsulation was completed by laminating a low-iron front glass with ethylene vinyl acetate (EVA) foil on top, producing a rigid module which can be placed into the window of the custom made PEC–PV cell. Current density *vs.* voltage (*J–V*) curves for solar cells were performed using a class-AAA, calibrated solar simulator operated at standard-test-conditions (STC, 25 °C, 1000 W m^{-2}). While energy conversion efficiencies of around 20% are normally achieved with the PVcomB process for non-cut, non-interconnected cells, the performance of the mini-modules here is considerably lower (Fig. S17 and Table S1†). This is due to (1) edge damage due to the laser cutting process, which degrades all *J–V* parameters in particular for such small cells, and (2) additional series resistances due to the cell interconnections, which reduce the fill factor. As a result, the mini modules exhibit conversion efficiencies in the range of 13–15% of 50 cm^2 under AM 1.5 G illumination.

13 PEC performance measurements

Large area BiVO$_4$ photoanodes were placed in a custom made cell[57] with an illumination area of 50 cm^2 (see Fig. S11, S18 and S19†), whilst small area devices were tested in a custom made

Teflon cell with an illumination area of 0.24 cm^2.[39] Photo-electrochemical measurements were conducted using an EG&G Princeton Applied Research 273A potentiostat in a three-electrode configuration with the $BiVO_4$ film as the working electrode, and an Ag/AgCl reference electrode (XR300, saturated KCl, Radiometer). A platinum wire was used as the counter electrode for small area cells, while two 2×10 cm^2 platinum coated mesh electrodes, one on either side of the working electrode, were used as counter electrodes for the large area devices. A WACOM Class AAA solar simulator (WXS-50S-5H) was used as the illumination source (AM1.5G, 100 mW cm^{-2}). This light source generates a collimated illumination area of 10×10 cm^2, in which only $\leq 2\%$ variation of the photon flux and power density was observed (see ESI Fig. S20 and Table S2†). KP_i buffer (pH 7) was used as the electrolyte for the PEC measurements with a concentration ratio of $KH_2PO_4 : K_2HPO_4$ of 1.63 : 1. To test for the influence of electrolyte conductivity on the PEC performance of the photoanode, different KP_i solutions consisting of a total phosphate concentration of 0.1–2.0 M (pH 7), and sodium sulfate (Na_2SO_4) solutions consisting of a total sulfate concentration of 0.125–2.0 M (pH 7) were used. The conductivity of electrolyte at each concentration was measured using a conductivity meter (LF 96, WTW). 0.1 M and 2.0 M KP_i electrolyte solutions were used for the PEC measurements of the small area and large area systems, respectively. In several PEC measurements, sodium sulfite (Na_2SO_3) was used as a hole scavenger. All measurements were conducted at room temperature with nitrogen gas bubbling through the electrolyte to agitate and remove the hydrogen and oxygen gases generated during illumination. All potentials were measured versus Ag/AgCl potential ($E_{Ag/AgCl}$) and converted to the reversible hydrogen electrode (RHE) scale using the Nernst equation:

$$E_{RHE} (V) = E_{Ag/AgCl} (V) + 0.0591 \times pH + E^0_{Ag/AgCl} \quad (2)$$

here, E_{RHE} is the applied potential versus RHE and $E^0_{Ag/AgCl}$ is the potential of the reference electrode (0.198 V_{RHE} at 25 °C). All $J–V$ curves were recorded with a scan rate of 10 mV s^{-1}.

Unassisted PEC–PV water splitting devices were characterized using the same large area custom-made PEC–PV cell. The cell consists of two windows at the front and rear with an illumination aperture of 50 cm^2. The system is designed in a modular fashion so that the 7×12 cm^2 front and rear quartz windows can be replaced with large area $BiVO_4$ photoanodes and/or the encapsulated 2 SHJ PV module. The Pt mesh counter electrodes were located in the same electrolyte compartment at both sides of the photoelectrode, so that they do not block the light path (see diagram in Fig. 8, S18 and S19†). The (photo)current and the voltage between the working and counter electrodes of the PEC–PV devices were measured with two Keysight 34461A digital multimeters.

Conflicts of interest

Four of the authors (I. A, Y. M, F. F. A and R. V. D. K) are named as inventors of international patent application WO 2019/052598 and German Patent Application DE 10 2017 121 228 A1, which are held by Helmholtz-Zentrum Berlin für

Materialien und Energie GmbH. The subject of the pre-treatment of FTO and electrochemical deposition of Ni bus-bars in the present publication partly covers the scope of the patent applications.

Acknowledgements

References

1 R. van de Krol and B. A. Parkinson, *MRS Energy and Sustainability*, 2017, **4**, E13.

2 Y. Park, K. J. McDonald and K.-S. Choi, *Chem. Soc. Rev.*, 2013, **42**, 2321–2337.

3 H. L. Tan, R. Amal and Y. H. Ng, *J. Mater. Chem. A*, 2017, **5**, 16498–16521.

4 T. W. Kim and K. S. Choi, *Science*, 2014, **343**, 990–994.

5 F. F. Abdi, L. Han, A. H. M. Smets, M. Zeman, B. Dam and R. van de Krol, *Nat. Commun.*, 2013, **4**, 2195.

6 F. F. Abdi, N. Firet and R. van de Krol, *ChemCatChem*, 2013, **5**, 490–496.

7 D. K. Zhong, S. Choi and D. R. Gamelin, *J. Am. Chem. Soc.*, 2011, **133**, 18370–18377.

8 Y. Pihosh, I. Turkevych, K. Mawatari, J. Uemura, Y. Kazoe, S. Kosar, K. Makita, T. Sugaya, T. Matsui, D. Fujita, M. Tosa, M. Kondo and T. Kitamori, *Sci. Rep.*, 2015, **5**, 11141.

9 F. F. Abdi, D. E. Starr, I. Y. Ahmet and R. van de Krol, *ChemPlusChem*, 2018, **83**, 941–946.

10 J. W. Ager, M. R. Shaner, K. A. Walczak, I. D. Sharp and S. Ardo, *Energy Environ. Sci.*, 2015, **8**, 2811–2824.

11 F. M. Toma, J. K. Cooper, V. Kunzelmann, M. T. McDowell, J. Yu, D. M. Larson, N. J. Borys, C. Abelyan, J. W. Beeman, K. M. Yu, J. Yang, L. Chen, M. R. Shaner, J. Spurgeon, F. A. Houle, K. A. Persson and I. D. Sharp, *Nat. Commun.*, 2016, **7**, 12012.

12 P. Bornoz, F. F. Abdi, S. D. Tilley, B. Dam, R. van de Krol, M. Grätzel and K. Sivula, *J. Phys. Chem. C*, 2014, **118**, 16959–16966.

13 L. Han, F. F. Abdi, R. van de Krol, R. Liu, Z. Huang, H.-J. Lewerenz, B. Dam, M. Zeman and A. H. M. Smets, *ChemSusChem*, 2014, **7**, 2832–2838.

14 Y.-S. Chen, J. S. Manser and P. V. Kamat, *J. Am. Chem. Soc.*, 2015, **137**, 974–981.

15 J. H. Kim, H. Kaneko, T. Minegishi, J. Kubota, K. Domen and J. S. Lee, *ChemSusChem*, 2016, **9**, 61–66.

16 X. Shi, K. Zhang, K. Shin, M. Ma, J. Kwon, I. T. Choi, J. K. Kim, H. K. Kim, D. H. Wang and J. H. Park, *Nano Energy*, 2015, **13**, 182–191.

17 X. Shi, H. Jeong, S. J. Oh, M. Ma, K. Zhang, J. Kwon, I. T. Choi, I. Y. Choi, H. K. Kim, J. K. Kim and J. H. Park, *Nat. Commun.*, 2016, **7**, 11943.

18 Y. Qiu, W. Liu, W. Chen, W. Chen, G. Zhou, P.-C. Hsu, R. Zhang, Z. Liang, S. Fan, Y. Zhang and Y. Cui, *Sci. Adv.*, 2016, **2**, e1501764.

19 Y. Peng, G. V. Govindaraju, D. K. Lee, K.-S. Choi and T. L. Andrew, *ACS Appl. Mater. Interfaces*, 2017, **9**, 22449–22455.

20 T. Higashi, H. Kaneko, T. Minegishi, H. Kobayashi, M. Zhong, Y. Kuang, T. Hisatomi, M. Katayama, T. Takata, H. Nishiyama, T. Yamada and K. Domen, *Chem. Commun.*, 2017, **53**, 11674–11677.

21 J. H. Baek, B. J. Kim, G. S. Han, S. W. Hwang, D. R. Kim, I. S. Cho and H. S. Jung, *ACS Appl. Mater. Interfaces*, 2017, **9**, 1479–1487.

22 W. Songcan, C. Peng, B. Yang, Y. Jung-Ho, L. Gang and W. Lianzhou, *Adv. Mater.*, 2018, **30**, 1800486.

23 L. Pan, J. H. Kim, M. T. Mayer, M.-K. Son, A. Ummadisingu, J. S. Lee, A. Hagfeldt, J. Luo and M. Grätzel, *Nat. Catal.*, 2018, **1**, 412–420.

24 B. Turan, J.-P. Becker, F. Urbain, F. Finger, U. Rau and S. Haas, *Nat. Commun.*, 2016, **7**, 12681.

25 K. Tolod, S. Hernández and N. Russo, *Catalysts*, 2017, **7**, 13.

26 N. Akihiro, O. Yasuyuki, K. Kayo, H. Yoshihide, N. Kensuke, S. Masakazu and F. Katsushi, *Appl. Phys. Express*, 2015, **8**, 107101.

27 J. Jia, L. C. Seitz, J. D. Benck, Y. Huo, Y. Chen, J. W. Ng, T. Bilir, J. S. Harris and T. F. Jaramillo, *Nat. Commun.*, 2016, **7**, 13237.

28 A. Hankin, F. E. Bedoya-Lora, C. K. Ong, J. C. Alexander, F. Petter and G. H. Kelsall, *Energy Environ. Sci.*, 2017, **10**, 346–360.

29 S. Haussener, C. Xiang, J. M. Spurgeon, S. Ardo, N. S. Lewis and A. Z. Weber, *Energy Environ. Sci.*, 2012, **5**, 9922–9935.

30 K. Walczak, Y. Chen, C. Karp, J. W. Beeman, M. Shaner, J. Spurgeon, I. D. Sharp, X. Amashukeli, W. West, J. Jin, N. S. Lewis and C. Xiang, *ChemSusChem*, 2015, **8**, 544–551.

31 H. Lu, V. Andrei, K. J. Jenkinson, A. Regoutz, N. Li, C. E. Creissen, A. E. H. Wheatley, H. Hao, E. Reisner, D. S. Wright and S. D. Pike, *Adv. Mater.*, 2018, **30**, 1804033.

32 S. Dilger, M. Trottmann and S. Pokrant, *ChemSusChem*, 2019, **12**, 1931–1938.

33 S. Wang, P. Chen, Y. Bai, J.-H. Yun, G. Liu and L. Wang, *Adv. Mater.*, 2018, **30**, 1800486.

34 Y. Ma, S. R. Pendlebury, A. Reynal, F. Le Formal and J. R. Durrant, *Chem. Sci.*, 2014, **5**, 2964–2973.

35 C. Carver, Z. Ulissi, C. K. Ong, S. Dennison, G. H. Kelsall and K. Hellgardt, *Int. J. Hydrogen Energy*, 2012, **37**, 2911–2923.

36 I. Holmes-Gentle, H. Agarwal, F. Alhersh and K. Hellgardt, *Phys. Chem. Chem. Phys.*, 2018, **20**, 12422–12429.

37 A. Luque and A. Marti, in *Handbook of Photovoltaic Science and Engineering*, ed. A. Luque and S. Hegedus, John Wiley & Sons, Ltd, Chichester, 2 edn, 2011, ch. 4, pp. 130–165.

38 M. A. Green, Y. Hishikawa, E. D. Dunlop, D. H. Levi, J. Hohl-Ebinger and A. W. Y. Ho-Baillie, *Prog. Photovoltaics Res. Appl.*, 2018, **26**, 3–12.

39 F. F. Abdi and R. van de Krol, *J. Phys. Chem. C*, 2012, **116**, 9398–9404.

40 C. Zachaus, F. F. Abdi, L. M. Peter and R. van de Krol, *Chem. Sci.*, 2017, **8**, 3712–3719.

41 J. A. Seabold and K.-S. Choi, *J. Am. Chem. Soc.*, 2012, **134**, 2186–2192.

42 D. K. Zhong, M. Cornuz, K. Sivula, M. Grätzel and D. R. Gamelin, *Energy Environ. Sci.*, 2011, **4**, 1759–1764.

43 T. H. Jeon, W. Choi and H. Park, *Phys. Chem. Chem. Phys.*, 2011, **13**, 21392–21401.

44 A. M. Ullman, C. N. Brodsky, N. Li, S.-L. Zheng and D. G. Nocera, *J. Am. Chem. Soc.*, 2016, **138**, 4229–4236.

45 R. C. Weast, *CRC Handbook of Chemistry, and Physics*, CRC Press, 70 edn, 1989.

46 C. H. Hamann, A. Hamnett and W. Vielstich, *Electrochemistry*, Wiley-VCH, New York, 2 edn, 2007.

47 T. Shinagawa, M. T.-K. Ng and K. Takanabe, *ChemSusChem*, 2017, **10**, 4155–4162.

48 M. A. Modestino, K. A. Walczak, A. Berger, C. M. Evans, S. Haussener, C. Koval, J. S. Newman, J. W. Ager and R. A. Segalman, *Energy Environ. Sci.*, 2014, **7**, 297–301.

49 E. A. Hernandez-Pagan, N. M. Vargas-Barbosa, T. Wang, Y. Zhao, E. S. Smotkin and T. E. Mallouk, *Energy Environ. Sci.*, 2012, **5**, 7582–7589.

50 A. Vilanova, T. Lopes and A. Mendes, *J. Power Sources*, 2018, **398**, 224–232.

51 J. Jin, K. Walczak, M. R. Singh, C. Karp, N. S. Lewis and C. Xiang, *Energy Environ. Sci.*, 2014, **7**, 3371–3380.

52 B. Pattengale and J. Huang, *Phys. Chem. Chem. Phys.*, 2016, **18**, 32820–32825.

53 F. W. P. Ribeiro, M. F. Gromboni, F. Marken and L. H. Mascaro, *Int. J. Hydrogen Energy*, 2016, **41**, 17380–17389.

54 J.-W. Jang, D. Friedrich, S. Müller, M. Lamers, H. Hempel, S. Lardhi, Z. Cao, M. Harb, L. Cavallo, R. Heller, R. Eichberger, R. van de Krol and F. F. Abdi, *Adv. Energy Mater.*, 2017, **7**, 1701536.

55 I. Y. Ahmet, R. van de Krol, F. F. Abdi and Y. Ma, *EP Pat.*, WO/2019/052598, 2019.

56 I. Y. Ahmet, R. van de Krol, F. F. Abdi and Y. Ma, *DE Pat.*, DE 10 2017 121 228 A1, 2019.

57 A. Vilanova, T. Lopes, C. Spenke, M. Wullenkord and A. Mendes, *Energy Storage Mater.*, 2018, **13**, 175–188.